Journal of Materials Chemistry A

Accepted Manuscript

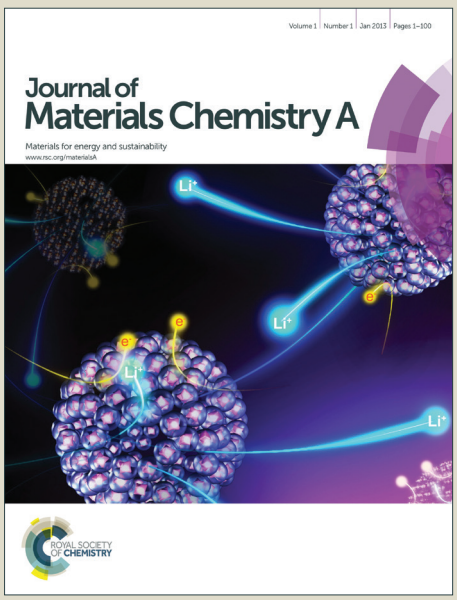

ROYAL SOCIETY OF CHEMISTRY

www.rsc.org/materialsA

Cite this: DOI: 10.1039/c0xx00000x

www.rsc.org/xxxxxx

ARTICLE TYPE

A facile synthesis of novel mesoporous Ge@C sphere anode: stable and high capacity for lithium ion batteries

Mingxian Liu, Xiaomei Ma, Lihua Gan,* Zijie Xu, Dazhang Zhu and Longwu Chen

Received (in XXX, XXX) Xth XXXXXXXXX 20XX, Accepted Xth XXXXXXXXX 20XX

DOI: 10.1039/b000000x

Tremendous volume expansion of germanium during cycling causes much difficulty to its use in high performance anodes for lithium ion batteries (LIBs). In this paper, we report a facile synthesis of novel mesoporous Ge@C spheres as stable and high capacity LIB anodes. Ge–catechol complex obtained *via* a simple chelation reaction was introduced into resorcinol/formaldehyde polymer spheres prepared by the extended Stöber method. After carbonization and carbothermic reduction at 800 °C in Ar atmosphere, carbon spheres loaded with Ge nanoparticles (~8 nm) were fabricated. The Ge/@C spheres have a uniform diameter of ~500 nm, a mesopore size of ~14 nm and a specific surface area of 348 m^2 g^{-1}. Mesoporosity between Ge particles and carbon matrix creates a buffer layer that effectively stabilizes the encapsulated Ge particles for huge volume change and mitigates the aggregation of active particles during the lithiation/delithiation process. Mesoporous Ge/@C sphere anode shows initial discharge and charge specific capacities of 1653 and 1440 mA h g^{-1} at 0.1 C. Even at a high rate of 10 C, the Ge@C electrode still has a reasonable discharge/charge specific capacity of 753/708 mA h g^{-1}, exhibiting excellent high-rate discharge–charge performance. The Ge/@C anode remains a high discharge capacity of 1099 mA h g^{-1} at 0.1 C with a coulombic efficiency of 99% after 100 cycles. The simple method for the design of mesoporous Ge@C spheres with a high capacity coupled with an excellent cycling stability opens up a new opportunity of Ge-based anode materials for widespread applications in LIBs.

Introduction

There has been an increasing research interest in the development of environmentally benign, long lifetime, low cost, renewable and high capacity batteries, especially reliable lithium-ion batteries (LIBs) with high energy and power density in popular consumer devices, such as mobile phones, laptops and hybrid electric vehicles.[1–5] Group IVA materials such as Si, Ge and Sn have been considered as promising anode materials for LIBs because of their high theoretical lithium-storage capacities.[6–9] For instance, silicon shows the highest theoretical gravimetric capacity of 4200 mA h g^{-1}, 11.3 times more than the commercial graphite anode which only has a theoretical capacity of 372 mA h g^{-1} [10, 11] Compared with Si, Ge has a much lower gravimetric capacity of 1600 mA h g^{-1}, but takes the advantage of better electrochemical kinetics associated with much higher lithium ion diffusivity (400 times higher than Si) and electronic conductivity (104 times higher than Si), which are the key factors in determining the rate capability of the anode.[7, 12, 13] Unfortunately, the tremendous volume expansion of Ge (also including Si and Sn) anode during charge–discharge (Li insertion–extraction) process results in severe pulverization and consequent poor cycling lifetime.[14–19] This disadvantage represents major obstacles to the development of germanium as commercial acceptable anode materials for LIBs. Therefore, it is important to design and synthesize Group IVA–based anode materials for finally reaching the point where high capacity and cycle stability become a reality.

Fortunately, recent efforts devoted to tailored nanostructures including nanowires, nanotubes, porous architectures, carbon nanocomposites and thin films have documented good cycling stability without compromising high capacities of the anodes.[20–27] For example, Paik group developed a group IVA based nanotube heterostructure array, consisting of a high–capacity Si inner layer and a highly conductive Ge outer layer, to yield both favorable mechanics and kinetics in LIB applications.[14] The Si/Ge double–layer nanotube array as a anode shows improved electrochemical performance including stable capacity retention (85% after 50 full cycles) and doubled capacity at a 3C rate. Han group designed amorphous hierarchical porous GeO_x began with the formation of germanate ions by the reaction of GeO_2 with NH_4OH, which was followed by reduction of these ions using $NaBH_4$.[20] The resultant GeO_x powders show a high capacity of ~1250 mA h g^{-1} for 600 cycles when used as anode for LIBs. The above–mentioned well–devoloped architectures effectively improve the electrochemical performance of Group IVA–based anode materials; however, to obtain high capacity coupled with long–term cyclical stability via a simple preparation process still remains a great challenge.

Graphite and carbon are the most actively used anode materials for commercial LIBs because of excellent electronic conductivity and cycle stability,[28–30] but suffer the disadvantage of low capacity. Ge nanoparticles, particularly when coated with carbons, are emerging as powerful anode materials for LIBs because carbon matrix is available for buffering the huge volume change and mitigating the aggregation of active particles during cycling.[13, 31–37] Meanwhile, carbon matrix could also increase the electronic conductivity of the electrodes.[38] Seng et al. reported the synthesis of GeO_2/Ge/C anode materials which is composed of GeO_2/Ge nanoparticles coated by a thin carbon layer, which is interconnected between neighboring particles to form clusters (~30 μm). [39] The GeO_2/Ge/C anode shows a high capacity of up to 1860 mA h g^{-1} and 1680 m Ah g^{-1} at 1 C and 10 C rates. Li et

al. used a tandem plasma reaction method to prepare ultrafine Ge nanoparticles embedded in carbon matrix.[37] Ge-C composite was deposited in a plasma reactor which consists of an inductive coil and a magnetron sputtering source. Ge particles were obtained by magnetron sputtering of a high purity Ge target, and then they were coated with carbon in the ICP zone by decomposition of CH_4. The Ge–C composite shows a lithium storage capacity of 980 mA h g^{-1} and excellent cycling performance.

Herein, we demonstrate a facial strategy for the design and synthesis of novel mesoporous Ge@C spheres as stable and high capacity anode materials for LIBs. Ge could form complex with oxygen-containing organic ligands, in particular with carboxylic acids and hydroxy acids.[40] Ge–catechol complex was obtained *via* a simple chelation reaction and then it was introduced into resorcinol/formaldehyde resin polymer spheres prepared by the extended Stöber method. After carbonization at 800 °C in Ar atmosphere, Ge/@C spheres (~500 nm in diameter) with Ge nanoparticles (~8 nm) enveloped within the carbon matrix were synthesized. On the one hand, the formation of complex between GeO_2 and catechol benefits the dispersion and encapsulation of GeO_2 into carbon spheres. On the other hand, the decomposition of the organic ligands chelate with GeO_2 and the carbothermic reduction of GeO_2 to Ge during carbonization at 800 °C generates mesopores (~14 nm) between the carbon matrix and Ge particles. The mesoporosity provides a buffer environment that effectively stabilizes the enveloped Ge particles for obvious volume change during cycling. As a result, mesoporous Ge/@C spheres as anode for LIBs show both high capacity and excellent cycling stability. Therefore, we believe that the simple method presented in this work highlights the great potential of Ge-based anode materials for widespread applications in LIBs.

Experimental section

Materials

Catechol, germanium dioxide powder (GeO_2, 99.99%), resorcinol, formaldehyde aqueous solution (37–40 wt%), ammonia solution (25 wt.%), ethanol and NaOH were purchased from Sinopharm Chemical Reagent Co., Ltd. Shanghai, China. Pure argon was provided by Shanghai BOC Special Gases Sales Service Co., Ltd. All chemicals were of analytical grade and were used as received without further purification. Water used was distilled water.

Synthesis of mesoporous Ge@C spheres

1.0 g of GeO_2 powder was mixed with 3.03 g of catechol and 47 mL water under stirring. NaOH solution was added to adjust the pH=10, then a transparent Ge–catechol complex was obtained, as shown in Scheme 1. Then, 100 mL of water, 40 mL of ethanol, 1.5 mL of ammonia solution and 1.0 g of resorcinol were mixed, and 15 mL of Ge–catechol complex was added. After stirring for 1.0 h, formaldehyde solution (1.4 mL) was added dropwise into the system with stirring for 24 h. The obtained Ge complex/ resorcinol–formaldehyde prepolymer was transferred into 100 mL Teflon container at 100 °C for 24 h to prepare Ge-containing polymer spheres. After dying at 100 °C and carbonization at 800 °C (3 °C min^{-1}) for 2 h under Ar atmosphere, mesoporous Ge@C spheres were obtained.

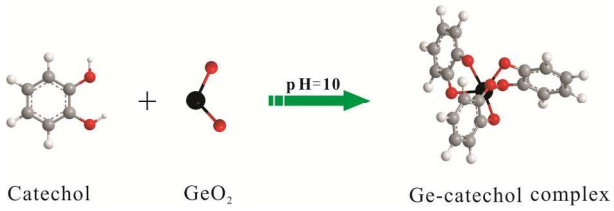

Scheme 1 Formation of Ge-catechol complex.

Characterization

Scanning electron microscopy (SEM) observations were taken on JSM-6700F equipment. Transmission electron microscopy (TEM) observations were done by JEM-2100 instrument operated at 200 kV. Before TEM characterization, the samples were dispersed in ethanol, and the suspensions of samples were dropped on a holey carbon coated copper grid. Nitrogen adsorption and desorption analysis was conducted on Micromeritics Tristar 3000 gas adsorption analyzer at –196 °C. Before tests, the samples were degassed at 200 °C under vacuum for more than 2 h. The specific surface area was calculated by Brunauer–Emmett–Teller (BET) method. The pore size distribution was estimated by Barrett–Joyner–Halenda (BJH) model by using the adsorption branch of the isotherms. The total pore volume was determined from the adsorbed amount at a relative pressure of P/P_0=0.98. Power X-ray diffraction (XRD) patterns were conducted on a Bruker Focus D8 diffract-meter with Cu Kα radiation (40 kV, λ=0.15418 nm) between 10 and 80°. Raman spectrum was recorded using Invia instrument with a 520 nm Ar-ion laser. X-ray photoelectron spectrum (XPS) measurement was carried out on an AXIS Ultra DLD spectrometer (Kratos) to investigate the surface elements composition. Thermogravimetric analysis (TGA) was done using a STA409 PC instrument under a static air atmosphere from room temperature to 900 °C at a heating rate of 15 °C min^{-1}.

Electrochemical Measurement

Electrochemical measurement was performed *via* two-electrode coin cell (CR2032 coin-type) using mesoporous Ge@C spheres as the working electrode and lithium foil as the counter electrode assembled in an argon-filled glove box. The working electrodes were prepared by mixing mesoporous Ge@C spheres, acetylene black and polyvinylidenefluoride (with a mass ratio of 8:1:1) in *N*-methylpyrrolidinone under vigorous stirring for 6 h to form slurry. The slurry was spread uniformly on a copper foil substrate and then dried at 120 °C in vacuum for 12 h. The circular electrode is 4 mg weight, 15 μm (thickness) ×1.2 cm (diameter). The electrolyte was 1 M $LiPF_6$ in a mixed solvent of ethylene carbonate, ethyl methyl carbonate and diethyl carbonate with a volume ratio of 1:1:1. The charge/discharge electrochemical performance of the electrodes was measured at 25 °C using an automatic battery testing system (LAND CT2001A) at a voltage window of 0.01–1.8 V. The specific capacity of electrode was calculated according to the weight of the active materials. The cell was tested after 2th, 50th and 100th cycles with the open circuit voltage maintaining at 1.8 V. Electrochemical impedance spectroscopy (EIS) (frequency range between 1 mHz and 10^3 kHz) was conducted on a CHI660D system.

Results and discussion

Scheme 2 shows schematic preparation of mesoporous Ge@C spheres, which is mainly based on chelation reaction and the extended Stöber method. The Stöber method has been most used to fabricate uniform colloidal silicon spheres by the hydrolysis and condensation of silica precursors.[41] Recently, Liu et al. first reported the extension of the Stöber method for the synthesis of resorcinol/formaldehyde resin polymer and carbon spheres with uniform and controllable diameters.[42] Stöber synthesis also offers new opportunities in preparation of micro- and/or mesoporous carbon spheres.[43–45] In the system of resorcinol–formaldehyde–water–ethanol–ammonia, emulsion droplets are formed through the H-bonding of resorcinol, formaldehyde, alcohol, and water. Resorcinol/formaldehyde polymerization takes place from the inside of emulsion droplets by ammonia catalysis, resulting in the formation of uniform polymer spheres.[42] On the other hand, GeO_2 could chelate with catechol by simple coordination reaction under base condition. Due to similar molecule structure and active sites between resorcinol and catechol, Ge–catechol complex is induced into emulsion droplets through aforementioned hydrogen bonding interaction, and then takes part in the polymerization reaction of resorcinol and formaldehyde, leading to the encapsulation of the Ge-containing complex into the polymer spheres. Mesoporous Ge@C spheres with Ge nanoparticles enveloped in the carbon matrix were fabricated by decomposition of catechol molecules chelate with GeO_2 and the conversion of GeO_2 to Ge during carbonization process (and carbothermic reduction) at 800 °C.[46] GeO_2 would cause the overall capacity fading and side reaction with lithium. Thus, thermal reduction of GeO_2 by magnesium, hydrogen, etc. under relatively high temperature (600 °C or above) or other mechanochemical reaction are required when GeO_2 was used as precursor.[30, 36] Our method combines the decomposition of the polymer spheres and the carbothermic reduction of GeO_2 to germanium during the carbonization process at 800 °C.

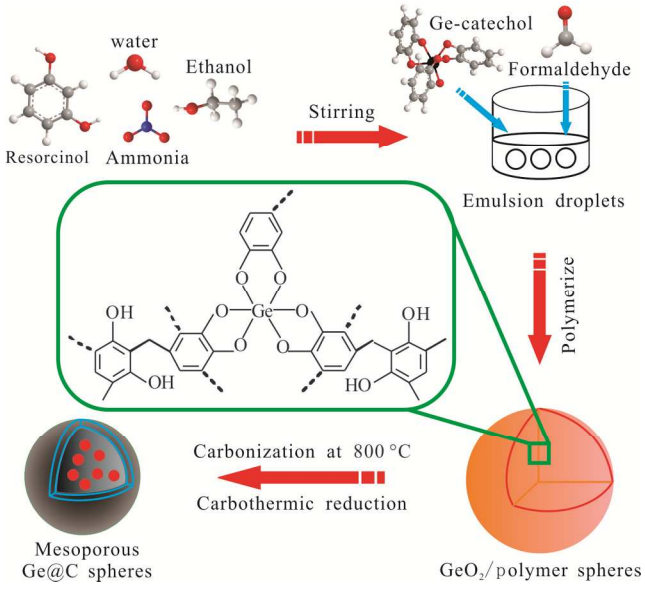

Scheme 2 Schematic synthesis route for mesoporous Ge@C spheres based on chelation reaction and the extended Stöber method.

XRD pattern of as-prepared mesoporous Ge@C spheres was shown in Fig. 1. The strong and well-defined diffraction peaks are assigned to the (111), (220), (311), (400) and (331) lattice planes of diamond cubic Ge (JCPDS card no. 04–0545).[33, 47] TGA image of mesoporous Ge/@C spheres was provided in Fig.2. The result shows that the mesoporous Ge/@C spheres comprises about 49 wt% Ge and 51 wt% carbon based on the weight loss upon carbon combustion and that Ge is fully oxidized to GeO_2 in air.

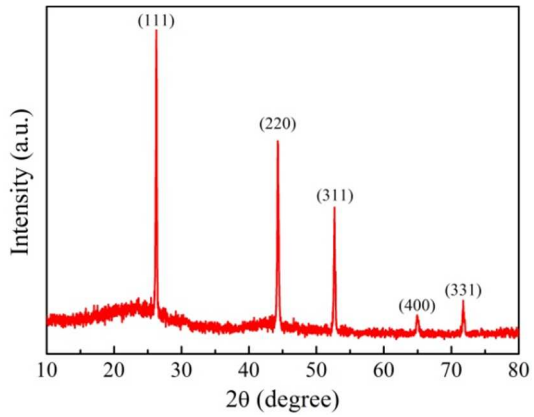

Fig. 1 XRD pattern of mesoporous Ge@C spheres.

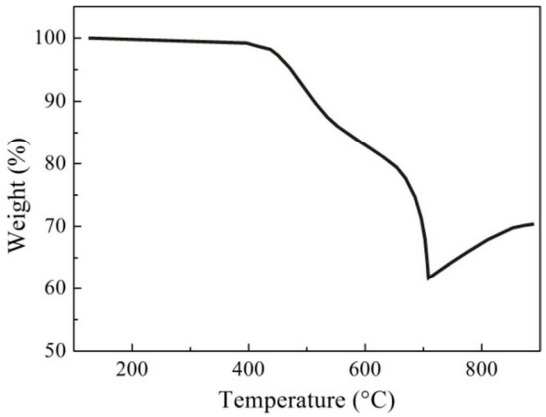

Fig. 2 TGA curve of mesoporous Ge@C spheres.

Raman spectra of mesoporous Ge@C spheres and GeO_2 are presented in Fig. 3. The Raman peak at 298 cm^{-1} indicates the optical mode of crystalline Ge.[47] The Raman spectrum of Ge@C spheres does not show any peak corresponding to GeO_2, which also suggests that Ge–catechol complex was transferred to Ge after carbonization and carbon reduction process at 800 °C, in agreement with the result of XRD analysis. Besides, there has a distinct pair of peaks located at about 1335 cm^{-1} (D band) and 1597 cm^{-1} (G band). The Raman D peak reflects a characteristic feature for disordered graphite or crystal defects, and the Raman G peak corresponds to an ideal graphitic lattice vibration mode with E_{2g} symmetry.[48] The ratio of the relative intensity of D band and G band (I_D/I_G) reflects the degree of graphitization, defects or the domain size of graphitization, i.e., the graphitization degree is in inverse ratio to the I_D/I_G value.[49] Generally, the I_D/I_G value for amorphous carbon is about 1.0.[50] The relative intensity ratio of I_D/I_G for Ge@C spheres is 0.85, suggesting that the carbon in the Ge@C composite comprises disorder carbon coupled with partial graphite layer, which would endow the consequent mesoporous

Ge@C sphere anode better electronic conductivity and enhanced electrochemical performance.

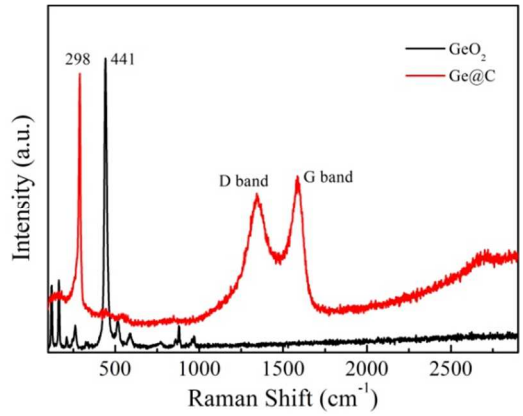

Fig. 3 Raman spectrum of mesoporous Ge@C spheres and GeO_2.

XPS spectrum of mesoporous Ge@C spheres shown in Fig.4a exhibits signals for the binding energy of Ge 3d, Ge 3p, Ge 3s, C 1s, O 1s, Ge $2p_{3/2}$ and Ge $2p_{1/2}$. While XPS spectrum of pure carbon spheres without Ge presents peaks corresponding to the binding energy of C 1s and O 1s. Fig. 4b shows a high–resolution XPS spectrum of Ge. The peak centered at 29.2 eV belongs to the binding energy of Ge 3d, and there is no binding energy of Ge–O detected at 33.2 eV. This result also suggests that the Ge–catechol complex was converted to Ge by carbothermic reduction process at 800 °C, in accordance with the results obtained from XRD and Raman characterization.

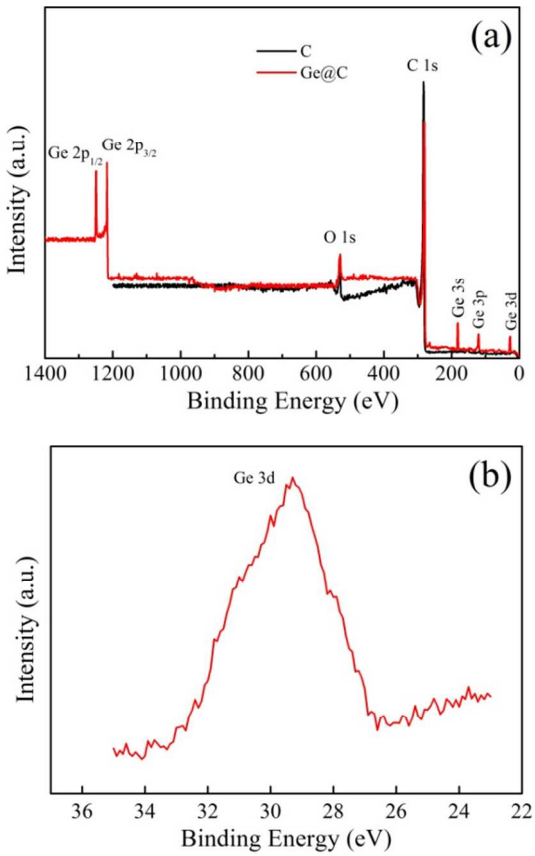

Fig. 4 Wide-scan XPS spectra of mesoporous Ge@C spheres and carbon spheres (a) and high–resolution XPS spectrum of Ge (b).

Fig. 5 shows SEM images of mesoporous Ge@C spheres. The Ge@C composite has regular spherical geometry with a uniform size, as shown in Fig.5a. The high-magnification SEM image (Fig. 5b) demonstrates that these Ge@C spheres have a mean diameter of about 500 nm, the same as that of carbon spheres prepared by using a similar procedure without Ge–catechol complex.[30, 51] A TEM image of the Ge@C spheres (Fig.6a) reflects similar sphere size with that of SEM characterization. A higher magnification TEM image of a region in Fig.6a shows that as-prepared Ge@C spheres have mesoporosity, as shown in Fig.6b. Fig.6c and Fig.6d give the TEM images of the fragments of Ge@C spheres, which clearly show the marked contrast between the Ge particles and the carbon; the dark cores correspond to Ge nanoparticles. Ge particles with a size of about 8 nm are well-embedded within the carbon matrix. The selected-area electron diffraction (SAED) pattern (Fig. 6c inset) reveals the (111), (220) and (311) planes of diamond cubic Ge,[33] which corresponds to the indexed diffraction peaks of Ge (111), (220) and (311) in XRD measurement shown in Fig. 1. A high-resolution transmission electron microscopy (HRTEM) image shown in the inset of Fig. 6d exhibits the highly ordered crystalline structure of the Ge nanoparticle with a (220) interplanar spacing (~0.2 nm).

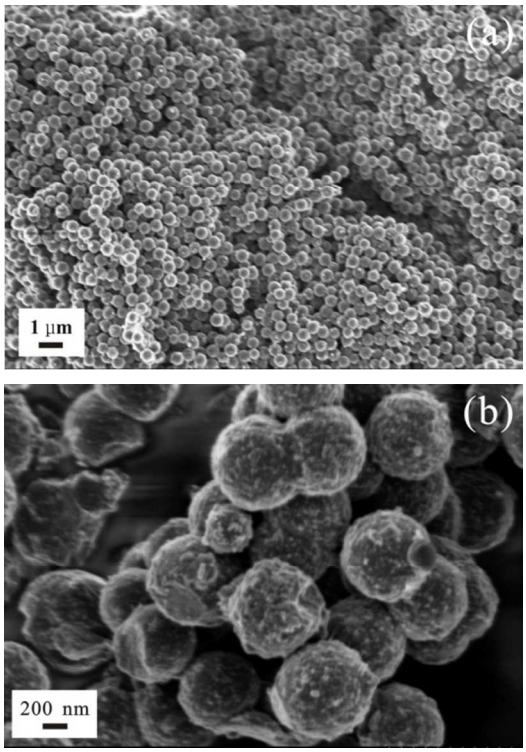

Fig.5 SEM images of mesoporous Ge@C spheres.

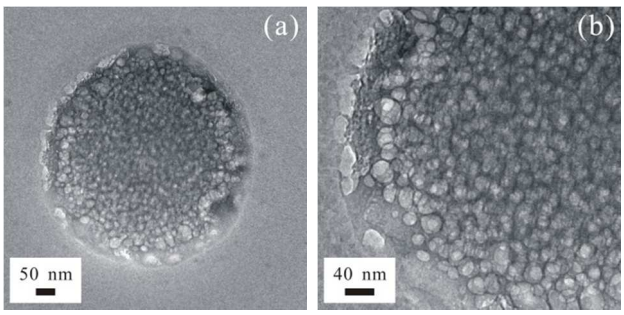

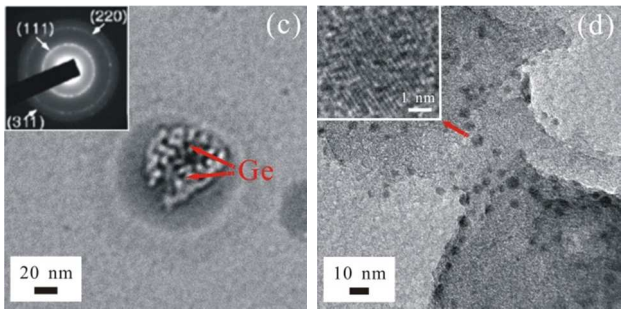

Fig.6 TEM images of mesoporous Ge@C spheres: (a) general image, (b) higher magnification image of a region in (a), (c) image of a fragment of a Ge@C sphere and SAED pattern of Ge phase (inset), and (d) image of a fragment of a Ge@C sphere and corresponding HRTEM image (inset).

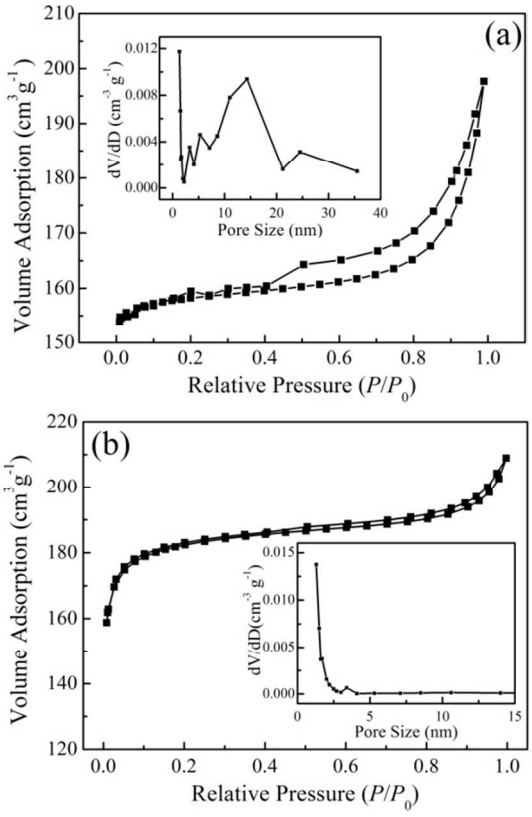

Fig. 7 Nitrogen absorption–desorption isotherms and pore size distributions of mesoporous Ge@C spheres (a) and pure carbon spheres (b).

Fig. 7a exhibits N_2 adsorption and desorption isotherms and corresponding pore size distribution curves of mesoporous Ge@C spheres. The adsorption–desorption isotherms of the Ge@C spheres are type IV profile with an obvious hysteresis loop at a relative pressure P/P_0 of 0.40–1.0, which is a typical feature of capillary condensation occurring in mesoporous solids. The mesoporous Ge@C spheres have a specific surface area of 348 m^2 g^{-1}. The pore size distribution curve shown in the inset of Fig. 5a indicates as-prepared Ge@C spheres have mesopores centered at 14 nm. As a comparison, pure carbon spheres were synthesized by using a similar procedure without Ge–catechol complex. N_2 adsorption and desorption isotherms of the pure carbon spheres indicates a microporous structure with a specific surface area of 476 m^2 g^{-1}, as shown in Fig.7b. The micropores in pure carbon spheres could be ascribed to the decomposition of resorcinol–formaldehyde resin polymer.[43] While the mesoporosity of Ge@C spheres results from the decomposition of catechol molecules chelate with GeO_2 and the carbothermic reduction of GeO_2 to Ge during high temperature carbonization at 800 °C. Generally, Ge undergoes a tremendous volume change of 370% during the Li ion insertion/extraction process, leading to the pulverization and capacity fading in bulk electrodes. Mesoporosity in the Ge@C carbon spheres yields enough void space (~14 nm) between Ge particles (~8 nm) and carbon matrix, which benefits for tolerating and buffering the huge volume change of Ge particles (expanded to ~12 nm) during the process of Li^+ intake/removal. Besides, this type of architecture can provide a large number of active sites for charge–transfer reactions, which is expected to endow the mesoporous Ge@C sphere anode with enhanced Li^+ storage capacity and improved rate capability.

Fig. 8 shows the discharge (lithium alloying) and charge (lithium dealloying) profiles of mesoporous Ge@C sphere anode at the first cycle. The anode shows an initial discharge and charge capacity of 1653 and 1440 mA h g^{-1} in the voltage range of 0.01–1.8 V *vs*. Li/Li$^+$ at a rate of 0.1 C (1 C=1600 mA g^{-1}) with a coulombic efficiency of 87%. For a comparison, pure carbon sphere anode shows a first discharge (charge) capacity of 496 (470 mA h g^{-1}) with a coulombic efficiency of 95%; while bared GeO_2 shows 1096/848 mA h g^{-1} in the first discharge/charge cycle with a coulombic efficiency of 77%. The initial irreversible capacity loss could mainly be ascribed to the electrochemical reduction of the electrolyte and the formation of solid electrolyte interface (SEI) film on the surface of the active Ge nanoparticles inside the mesopores and/or irreversible lithium insertion into the host materials.[39, 52–54] Compared with bared GeO_2, mesoporous Ge@C sphere anode shows improved discharge–charge capacity and coulombic efficiency, which should originate from the reduction of GeO_2 to nanoscaled Ge particles and the additional carbon phase which provides the well conductivity.

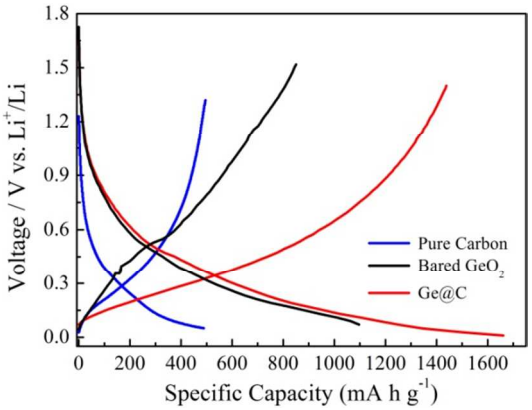

Fig. 8 First discharge–charge profiles of mesoporous Ge@C spheres, pure carbon and bared GeO_2.

Fig. 9a shows the initial specific discharge–charge capacity vs. voltage profiles of mesoporous Ge@C sphere anode at various rates of 0.1–10 C. Even at a high rate of 10 C, the mesoporous Ge@C sphere anode still remains a reasonable discharge/charge specific capacity of 753/708 mA h g^{-1}, exhibiting excellent high-

rate discharge–charge performance. The rate capability of the anode material is very important especially for the applications in electric vehicles.[55] The specific capacity and cycling performance of the Ge@C sphere anode under different rates within 10 cycles are shown in Fig. 9b. The discharge or charge specific capacity decreases upon increasing the current densities from 0.1 to 10 C. Importantly, after the high-rate measurements, the specific capacity of the Ge@C sphere anode reversibly recovers to 1338 mA h g^{-1} once the rate goes back to 0.1 C, indicating a good electrochemical reversibility and structural integrity. This has been well-studied in carbon, Si, and/or Ge electrodes. [17, 33, 39, 56]

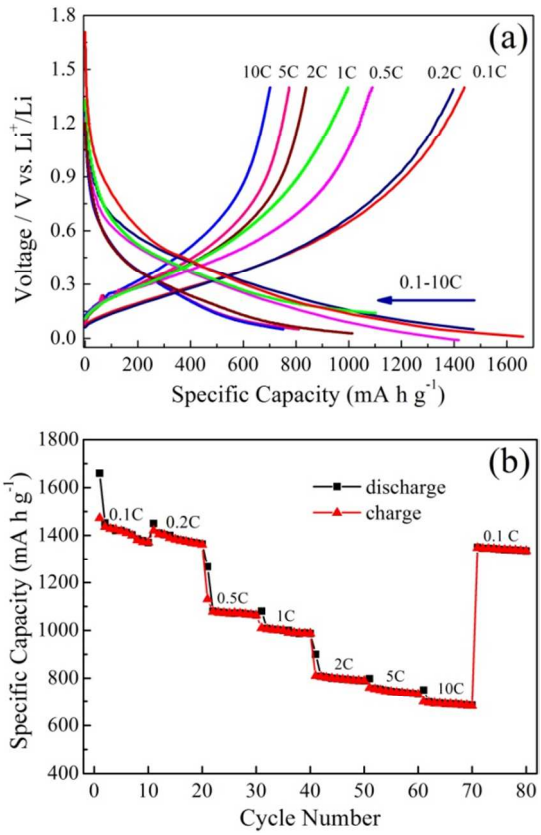

Fig.9 Initial discharge/charge capacity curves (a) and cycling performance (b) of mesoporous Ge@C sphere anodes at 0.1–10 C.

Long-term discharge–charge capacity and columbic efficiency of mesoporous Ge@C sphere anode at 0.1 C are shown in Fig.10. In the first discharge–charge process, mesoporous Ge@C sphere anode shows irreversible capacity loss due to the formation of SEI films. Mesoporous Ge@C sphere anode remains 98% columbic efficiency and a discharge specific capacity 1099 mA h g^{-1} after 100 cycles, higher than that of pure Ge (~600 mA h g^{-1} at 200 mA g^{-1}, 15 cycles),[57] mesoporous carbon spheres (327 mA h g^{-1} at 50 mA g^{-1}, 30 cycles),[30] hierarchically porous germanium-modified carbon (545 mA h g^{-1} at 150 mA g^{-1}, 30 cycles),[36] Ge@C/RGO nanocomposites (~940 mA h g^{-1} at 50 mA g^{-1}, 50 cycles),[33] and the Ge/C composite (~900 mA h g^{-1} at 150 mA g^{-1}, 50 cycles).[41] The mesoporosity between carbon matrix and Ge nanoparticles provides an environment that effectively stabilizes the enveloped Ge particles and buffer the mechanical stress of the anode caused by the large volumetric change during discharge–charge cycle process, and thus endows mesoporous Ge@C sphere anode high specific capacity and excellent cyclic stability.

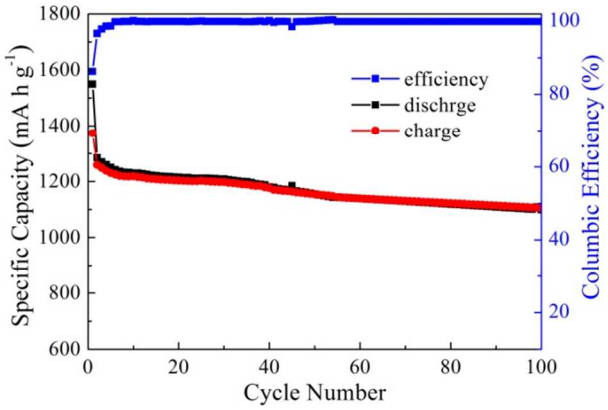

Fig. 10 Long-term discharge–charge capacity and columbic efficiency of mesoporous Ge@C sphere anode at 0.1 C.

EIS measurement could reflect the charge transfer resistance of the anode.[58–61] Fig. 11 shows Nyquist plots of mesoporous Ge@C sphere anode before and after long-term discharge–charge cycles. Nyquist plots of the Ge@C sphere anode show semicircles in high frequency range and linear tails in low frequency region. The semicircles reflect the interface resistance of mesoporous Ge@C sphere anode, which is associated with the SEI film and charge transfer resistance of Li-ion insertion.[58] The linear tails in low frequency region is assigned to the diffusion of Li-ions in the andoe.[59] Mesoporous Ge@C sphere anode after 50 cycles shows a slightly increasing semicircle, indicating no obvious change of the charge transfer resistance of Li ions from and into the electrode. After 100 cycles at 0.1 C, the charge transfer resistance was about 78 Ω, much lower than that of pure Ge (~600 Ω), as shown in the inset of Fig.11. Low charge transfer resistance is beneficial to the Li ion transfer at the interface of the electrolyte/electrode for the well cycle performances.

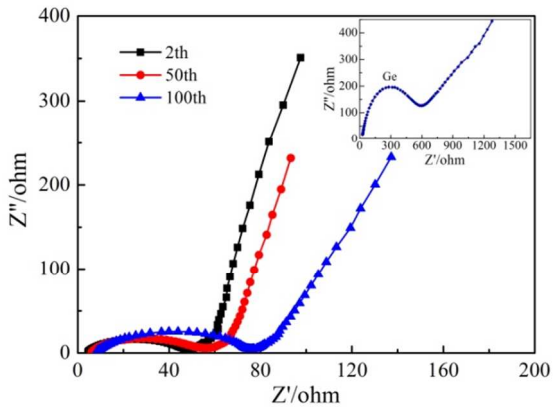

Fig. 11 Nyquist plots of mesoporous Ge@C sphere anode after 2, 5 and 100 cycles. The inset shows Nyquist plots of pure Ge.

Conclusions

In conclusion, we describe a facile design and synthesis of novel mesoporous Ge@C spheres based on simple chelation reaction and the extended Stöber method. The Ge/@C spheres show a uniform diameter of ~500 nm, a mesopore size of ~14 nm, and a

specific surface area of 348 m^2 g^{-1}. Mesoporosity between Ge nanoparticles (~8 nm) and the carbon matrix generates an environment that effectively stabilizes the enveloped Ge particles and buffers the mechanical stress of the active materials caused by huge volumetric change during long-term discharge–charge process. Mesoporous Ge@C sphere anode shows initial discharge and charge specific capacities of 1653 and 1440 mA h g^{-1} at 0.1 C . It still has a reasonable discharge/charge specific capacity of 753/708 mA h g^{-1} even at a high rate of 10 C, exhibiting excellent high-rate discharge–charge performance. The Ge/@C electrode remains a high discharge capacity of 1099 mA h g^{-1} at 0.1 C with a coulombic efficiency of 99% after 100 cycles. The simple method for the development of mesoporous Ge@C spheres with both high capacity and excellent cycling stability highlights the promising potential of Ge-based anode materials for widespread applications in LIBs.

Acknowledgments

This work was financially supported by the National Natural Science Foundation of China (21207099, 21273162, 21473122), the Science and Technology Commission of Shanghai Municipality, China (11nm0501000, 12ZR1451100), and the Large Equipment Test Foundation of Tongji University (2013063, 2013069).

Notes and references

Department of Chemistry, Tongji University, 1239 Siping Road, Shanghai 200092, P. R. China. Fax: 86 21 65981097; Tel: 86 21 65982654-8430; E-mail: ganlh@tongji.edu.cn

† Electronic Supplementary Information (ESI) available. See DOI: 10.1039/b000000x/

1 M. Armand and J.-M. Tarascon, *Nature*, 2008, **451**, 652–657.
2. J. B. Goodenough and Y. Kim, *Chem. Mater.*, 2010, **22**, 587–603.
3. J.-Y. Luo, W.-J. Cui, P. He and Y.-Y. Xia, *Nat. Chem.*, 2010, **2**, 760–765.
4. Z. Wang, Z. Wang, W. Liu, W. Xiao and X. W. Lou, *Energy Environ. Sci.*, 2013,**6**, 87–91.
5. S. Chen, Y. Xin, Y. Zhou, Y. Ma, H. Zhou and L. Qi, *Energy Environ. Sci.*, 2014, **7**, 1924–1930.
6. J. Zhu, D. Wang, L. Cao and T. Liu, *J. Mater. Chem. A*, 2014, DOI: 10.1039/C4TA02021A.
7. T. Song, Y. Jeon, M. Samal, H. Han, H. Park, J. Ha, D. K. Yi, J.-M. Choi, H. Chang, Y.-M. Choi and U. Paik, *Energy Environ. Sci.*, 2012, **5**, 9028–9033.
8. C. K. Chan, H. Peng, G. Liu, K. Mcilwrath, X. F. Zhang, R. A. Huggins and Y. Cui, *Nat. Nanotech*., 2008, **3**, 31–35.
9. Y.-S. Hu, R. Demir-Cakan, M.-M. Titirici, J.-O. Müller, R. Schlögl, M. Antonietti and J. Maier, *Angew. Chem. Int. Ed.*, 2008, **47**, 1645–1649.
10 S. Chu and A. Majumdar, *Nature*, 2012, **488**, 294–303.
11 P. G. Bruce, B. Scrosati and J.-M. Tarascon, *Angew. Chem. Int. Ed.*, 2008, **47**, 2930–2946.
12 J. Cheng and J. Du, *CrystEngComm*, 2012, **14**, 397–400.
13 D. D. Vaughn II and R. E. Schaak, *Chem. Soc. Rev.*, 2013, **42**, 2861–2869.
14 T. Song, H. Cheng, H. Choi, J.-H. Lee, H. Han, D. H. Lee, D. S. Yoo, M.-S. Kwon, J.-M. Choi, S. G. Doo, H. Chang, J. Xiao, Y. Huang, W. Il Park, Y.-C. Chung, H. Kim, J. A. Rogers and U. Pai, *ACS Nano*, 2012, **6**, 303–309.
15 H. Zhang and P. V. Braun, *Nano Lett*., 2012, **12**, 2778–2783.
16 A. Esmanski and G. A. Ozin, *Adv. Funct. Mater.*, 2009, **19**, 1999–2010.
17 H. Wu, G. Chan, J. W. Choi, I. Ryu, Y. Yao, M. T. McDowell, S. W. Lee, A. Jackson, Y. Yang, L. B. Hu and Y. Cui, *Nat. Nanotechnol.*, 2012, 7, 310–315.
18 A. M. Chockla, J. T. Harris, V. A. Akhavan, T. D. Bogart, V. C. Holmberg, C. Steinhagen, C. B. Mullins, K. J. Stevenson and B. A. Korgel, *J. Am. Chem. Soc.*, 2011, **133**, 20914–20921.
19 K. Oma, M. Herstedt and D. Abraham, *J. Power Sources*, 2006, **153**, 380–384.
20 X.-L. Wang, W.-Q. Han, H. Chen, J. Bai, T. A. Tyson, X.-Q. Yu, X.-J. Wang and X.-Q. Yang, *J. Am. Chem. Soc.*, 2011, **133**, 20692–20695.
21 X. Hou, H. Jiang, Y. Hu, Y. Li, J. Huo and C. Li, *ACS Appl. Mater. Interfaces*, 2013, **5**, 6672–6677.
22 M. H. Park, K. Kim, J. Kim and J. Cho, *Adv. Mater.* 2010, **22**, 415–418.
23 J. Hassoun, S. Panero, P. Simon, P. L. Taberna and B. Scrosati, *Adv. Mater.* 2007, **19**, 1632–1635.
24 G. Derrien, J. Hassoun, S. Panero and B. Scrosati, *Adv. Mater.*2007, **19**, 2336–2340.
25 Y. Yu, L. Gu, C. L. Wang, A. Dhanabalan, P. A. van Aken and J. Maier, *Angew. Chem., Int. Ed.* 2009, **48**, 6485–6489.
26 A. Magasinski, P.Dixon, B. Hertzberg, A. Kvit, J. Ayala and G. Yushin, *Nat. Mater.* 2010, **9**, 353–358.
27 B. Hertzberg, A. Alexeev and G.Yushin, *J. Am. Chem. Soc.* 2010, **132**, 8548–8549.
28 H.-C. Shin and M. Liu, *Adv. Funct. Mater*., 2005, **15**, 582–586.
29 X. H. Liu, S. Huang, S. T. Picraux, J. Li, T. Zhu and J. Y. Huang, *Nano Lett.*, 2011, **11**, 3991–3997.
30 X. Ma, M. Liu, L. Gan, P. K. Tripathi, Y. Zhao, D. Zhu, Z. Xu and L. Chen, *Phys. Chem. Chem. Phys.*, 2014, **16**, 4135–4142.
31 Y.-G. Guo, J.-S. Hu and L.-J. Wan, *Adv. Mater.*, 2008, **20**, 2878–2887.
32 J.-G. Ren, Q.-H. Wu, H. Tang, G. Hong, W. Zhang and S.-T. Lee, *J. Mater. Chem. A*, 2013, **1**, 1821–1826.
33 D. J. Xue, S. Xin, Y. Yan, K. C. Jiang, Y. X. Yin, Y. G. Guo and L. J. Wan, *J. Am. Chem. Soc.*, 2012, **134**, 2512–2515.
34 B. Li, H. Cao, J. Shao and M. Qu, *Chem. Commun.*, 2011, **47**, 10374–10376.
35 M.-H. Seo, M. Park, K. T. Lee, K. Kim, J. Kim and J. Cho, *Energy Environ. Sci.*, 2011, **4**, 425–428.
36 Y. Xiao, M. Cao, L. Ren and C. Hu, *Nanoscale*, 2012, **4**, 7469–7474.
37 W. Li, J. Zheng, T. Chen, T. Wang, X. Wang and X. Li, *Chem. Commun.*, 2014, **50**, 2052–2054.
38 X. Han, G. Qing, J. Sun and T. Sun, *Angew. Chem. Int. Ed.*, 2012, **51**, 1–5.
39 K. H. Seng, M.-H. Park, Z. P. Guo, H. K. Liu and J. Cho, *Nano Lett.*, 2013, **13**, 1230–1236.

40 J. P. Marco-Lozar, D. Cazorla-Amorös and A. Linares-Solano, *Carbon*, 2007, **45**, 2519–2528.

41 W. Stöber, A. Fink and E. J. Bohn, *J. Colloid Interface Sci.*, 1968, **26**, 62–69.

42 J. Liu, S. Z. Qiao, H. Liu, J. Chen, A. Orpe, D. Zhao and G. Q. Max Lu, *Angew. Chem., Int. Ed.*, 2011, **50**, 5947–5951.

43 J. Choma, D. Jamioła, K. Augustynek, M. Marszewski, M. Gao and M. Jaroniec, *J. Mater. Chem.*, 2012, **22**, 12636–12642.

44 J. Qian, M. Liu, L. Gan, P. K. Tripathi, D. Zhu, Z. Xu, Z. Hao, L. Chen and D. S. Wright, *Chem. Commun.,* 2013, **49**, 3043–3045.

45 X. Ma, L. Gan, M. Liu, P. K. Tripathi, Y.Zhao, Z. Xu, D. Zhu and L. Chen, *J. Mater. Chem. A*, 2014, **2**, 8407–8415.

46 M. Halmann, A. Frei and A. Steinfeld, *Miner. Process. Extr. Metall. Rev.*, 2011, **32**, 247−266.

47 G. Cui, L. Gu, L. Zhi, N. Kaskhedikar, P. A. van Aken, K. Müllen and J. Maier, *Adv. Mater.*, 2008, **20**, 3079–3083.

48 A. Sadezky, H. Muckenhuber, H. Grothe, R. Niessner and U. Pöschl, *Carbon*, 2005, **43**, 1731–1742.

49 W. Gao, Y. Wan, Y. Dou and D. Zhao, *Adv. Energy Mater.*, 2011, **1**, 115–123.

50 M. Liu, L. Gan, W. Xiong, Z. Xu, D. Zhu and L. Chen, *J. Mater. Chem. A*, 2014, **2**, 2555–2562.

51 X. Ma, M. Liu, L. Gan, Y. Zhao, L. Chen, *J. Solid State Electrochem.*, 2013, **17**, 2293–2301.

52 M. Ahmad, Y. Shi, A. Nisar, H. Sun, W. Shen, M. Wei and J. Zhu, *J. Mater. Chem.*, 2011, **21**, 7723–7729.

53 G. Jo, I. Choi, H. Ahn and M. J. Park, *Chem. Commun.*, 2012, **48**, 3987–3989.

54 J. Deng, H. Ji, C. Yan, J. Zhang, W. Si, S. Baunack, S. Oswald, Y. Mei and O. G. Schmidt, *Angew. Chem. Int. Ed.*, 2013, **52**, 2326–2330.

55 W. Tang, L. Liu, Y. Zhu, H. Sun, Y. Wu and K. Zhu, *Energy Environ. Sci.*, 2012, **5**, 6909−6913.

56 K. H. Seng, M.-H. Park, Z. P. Guo, H. K. Liu and J. Cho, *Angew. Chem. Int. Ed.*, 2012, **51**, 5657–5661.

57 J. Cheng and J. Du, *CrystEngComm*, 2012, **14**, 397–400.

58 J. Guo, A. Sun, X. Chen, C. Wang and A. Manivannan, *Electrochim. Acta*, 2011, **56**, 3981–3987.

59 R. Ruffo, S. S. Hong, C. K. Chan, R. A. Huggins and Y. Cui, *J. Phys. Chem. C*, 2009, **113**, 11390–11398.

60 L. P. Tan, Z. Lu, H. T. Tan, J. Zhu, X. Rui, Q. Yan and H. H. Hng, *J. Power Sources*, 2012, 206, 253–258.

61 W. Li, X. Wang, B. Liu, S. Luo, Z. Liu, X. Hou, Q. Xiang, D. Chen and G. Shen, *Chem. Eur. J.*, 2013, **19**, 8650–8656.

Graphical Abstract

A facile synthesis of mesoporous Ge@C sphere anode: stable and high capacity for lithium ion batteries

Mingxian Liu, Xiaomei Ma, Lihua Gan,* Zijie Xu, Dazhang Zhu and Longwu Chen.

A facial synthesis of mesoporous Ge@C spheres as stable and high capacity anode for lithium ion batteries is described.